

# Influence of microstructure topography on the oblique impact dynamics of drops on superhydrophobic surfaces

*Damon G. K. Aboud, Anne-Marie Kietzig\**

Department of Chemical Engineering, McGill University, Montreal QC, H3A 0C5 Canada

## KEYWORDS

Drops, wetting, drop impact, oblique drop impact, superhydrophobicity, Weber number, oblique impact, inclined surface, drop rebound, contact time, coefficient of restitution, angle of incidence.

## ABSTRACT

This report investigates the influence of microstructure topography on the restitution coefficient, maximum spreading diameter, and contact time of oblique drop impacts on superhydrophobic surfaces. The 5 surfaces tested allow for comparison of open- vs. closed-cell structures, feature size and spacing, and hierarchical vs. nanoscale-only surface structures. By decoupling the restitution coefficient into a normal ( $\varepsilon_n$ ) and tangential component ( $\varepsilon_t$ ), it is demonstrated that both  $\varepsilon_n$  and  $\varepsilon_t$  are largely independent of the microstructure topography. Instead, the restitution coefficient is governed almost exclusively by the normal Weber number. Next, a new model is

presented that relates the maximum spreading diameter to an adhesion coefficient that characterizes the overall adhesive properties of the superhydrophobic microstructure during drop rebounding. Through this analysis, we discovered that surface geometries with greater microstructure roughness (i.e. overall surface area) promote a higher maximum spreading diameter than flatter geometries. Furthermore, the contact time of drop impacts on flat surfaces is positively correlated with the impact velocity, due to penetration of the liquid into the porous nanostructure. However, this trend reverses for oblique impacts due to the presence of stretched rebounding behaviour. Finally, substrates patterned with sparse pillar microstructures can exhibit pancake bouncing behaviour, resulting in extremely low contact times. This unique bouncing mechanism also significantly influences the restitution coefficient and spreading diameter of oblique impacts.

## INTRODUCTION

In recent years, superhydrophobic surfaces have attracted a lot of scientific interest, owing to their unique ability to completely reflect water drops. Accordingly, superhydrophobic surfaces are an attractive technology for applications such as anti-icing turbine blades and electrical cables [1], and water-shedding windows [2]. However, the design of superhydrophobic surfaces for such applications first requires a fundamental understanding of single drop impacts. Hence, in this report, we measure and compare the restitution coefficient, contact time, and spreading diameter of oblique drop impacts on five different superhydrophobic surfaces.

A superhydrophobic surface is defined by having an advancing contact angle ( $\theta_A$ ) greater than  $150^\circ$ , and very low contact angle hysteresis (CAH) [3]. These properties are characteristic for surfaces which trap pockets of air within their pores, so that when a water drop impacts the surface, it makes physical contact only with the topographical peaks of the structure and is

otherwise suspended over air. This non-wetting phenomenon, known as the Cassie wetting state, results in drops rebounding off the surface entirely [4].

Drop impacts are best characterized in terms of the normal Weber number,  $We_n = \rho v_{n1}^2 D_0 / \sigma$ , where  $\rho$  is the density of the liquid,  $v_{n1}$  is the initial normal velocity of impact,  $D_0$  is the initial drop diameter, and  $\sigma$  is the liquid's surface tension. The Weber number gives a dimensionless comparison between the drop's kinetic energy and its surface tension. The Weber number was selected as the governing parameter for this report because it has been shown to effectively scale both the spreading [5] and rebounding [6] behaviour of drops rebounding on solid surfaces. Furthermore, throughout this report our results will be mainly presented in dimensionless format, where a star superscript after a variable indicates the dimensionless version. Thus, the dimensionless maximum spreading diameter is given by  $D_{max}^* = D_{max} / D_0$ , where  $D_{max}$  is the actual maximum spreading diameter in millimeters. Similarly, the dimensionless time is calculated

with respect to the inertial-capillary time  $\tau_{ic} = \sqrt{\rho D_0^3 / 8\sigma}$ , such that  $t^* = t / \tau_{ic}$ .

When a water drop impacts a superhydrophobic surface, the liquid expands and flattens into a disk shape as the drop's initial kinetic energy is transferred into surface energy. Eventually, the drop reaches its maximum spreading diameter, and surface tension begins to pull the liquid back towards the drop's center. During this retraction phase, surface energy is transferred back into kinetic energy, leading the drop to push off the superhydrophobic surface and completely rebound. Energetically, this rebounding process is not ideal. During the expansion and retraction phases, some kinetic energy is lost due to viscous dissipation. And, as the drop rebounds, much of the liquid's kinetic energy is transferred into vibrational modes [7]. Accordingly, the final velocity of the drop as it detaches from the surface ( $v_2$ ) is always lower than the initial impact velocity

( $v_1$ ). The restitution coefficient  $\varepsilon = v_2/v_1 < 1$  provides a useful characterization of the energy losses during the rebound process and has applications in the field of microfluidics.

The contact time ( $t_c$ ) of a rebounding drop is important for modeling the heat transfer kinetics when a drop impacts a hot or cold superhydrophobic surface [8]. Previous experiments have found that, regardless of  $v_n$ , the dimensionless contact time  $t_c^* = t_c/\tau_{ic}$  is consistently equal to around 2.60 for normal drop impacts [6, 9], but can vary significantly depending on certain factors. Notably, Liu et al. (2014) discovered a unique form of drop rebounding called pancake bouncing, which can reduce  $t_c^*$  to as low as 0.53, and typically occurs on superhydrophobic surfaces that have a pillared microstructure, with pillar spacing over 200  $\mu\text{m}$  [10]. Immediately upon impact, the liquid penetrates the wide pores between the pillars, but is quickly ejected due to the antiwetting pressure of the liquid-air interface. Pancake bouncing occurs when this capillary ejection transpires before the retraction phase begins and has enough force to lift the drop off the surface. This causes the drop to detach at a very early time, while still outstretched in a pancake shape [10].  $t_c^*$  is also influenced by drop pinning, which is caused by the high dynamic pressure ( $P_d \propto \rho v_{n1}^2$ ) the liquid drop exerts on the surface in high-speed impacts [11]. Hence, any impact with a sufficiently high  $P_d$  will cause the liquid to completely fill the surface features and expel the air pockets that define the Cassie wetting state [12]. This alternate wetting state is known as Wenzel wetting, and results in much more area of solid-liquid contact, causing the liquid drop to become firmly attached to the superhydrophobic surface [13]. Naturally, this firm attachment increases the length of  $t_c^*$ , and also leads to partial rebounding behaviour, where a small secondary drop remains attached to the surface as the rest of the liquid bounces away.

Another important characteristic of drop impacts is the dimensionless maximum spreading diameter ( $D_{max}^* = D_{max}/D_0$ ) of the lamella at the end of the expansion phase. Industrially, the

prediction of  $D_{max}^*$  is crucial towards understanding the adhesion present between the drop and surface [8]. For impacts on flat surfaces, many correlations have been proposed to model the dimensionless maximum spreading diameter of normal drop impacts ( $D_{n,max}^*$ ), but most follow the general format:

$$D_{n,max}^* = a \cdot We_n^b \quad \text{Equation 1}$$

where  $a$  and  $b$  are fitting factors. Some examples of published correlations are  $D_{n,max}^* = 0.9 \cdot We_n^{0.25}$  [5], and  $D_{n,max}^* = 0.72 \cdot We_n^{0.29}$  [14].

In previous reports, we modeled the restitution coefficient ( $\epsilon$ ), contact time ( $t_c^*$ ), and maximum spreading diameter ( $D_{max}^*$ ) of oblique drop impacts on a single superhydrophobic surface [14, 15]. In this study, we broaden the application of those findings by testing 5 different superhydrophobic surfaces. One surface is covered only in a superhydrophobic nanostructure, whereas the other four samples are hierarchical, consisting of a microstructure (pillars, holes, or wavy trenches) that is in turn covered with the same nanostructure. These choices of geometry allow us to compare open- and closed-cell structures (pillars versus holes), features with varying peak-to-peak spacing (ranging from 10 to 200  $\mu\text{m}$ ), and the difference between hierarchical and single-scale superhydrophobic surfaces. The goal of this study is to identify the microstructure's influence on the impact dynamics, so that the behaviour of impacting drops can be successfully predicted for a wide range of different superhydrophobic surfaces.

## EXPERIMENTAL

All 5 sample surfaces were fabricated via femtosecond laser micromachining. This fabrication method was selected because it is a one-step, scalable method of producing hierarchical micro/nanostructures, and therefore represents a realistic method of producing superhydrophobic

surfaces for industrial applications. PTFE was selected as the base material due to its inherent hydrophobicity. Using dynamic contact angle goniometry, we measured an advancing contact angle of  $\theta_A = 116.1^\circ$  and a receding contact angle of  $\theta_R = 84.9^\circ$  on our polished PTFE blanks, indicating hydrophobic behaviour. To fabricate our sample surfaces, a Coherent Libra amplified Ti:Sapphire laser with a repetition rate of 1 kHz and a pulse duration <100 fs was used. Its beam was focused using a 100 mm lens to irradiate square coupons of flat PTFE. The lasing parameters of the Wavy sample have been described previously [16]. To develop the other microstructures, custom Python codes were used to control the complex raster scanning trajectories executed by a 3-dimensional translation stage. Using a pulse peak fluence of 46 J/cm<sup>2</sup> and a 70% line overlap, the beam selectively ablated the polymer, resulting in an array of pillar or hole microstructures. Then, the entire sample area was micromachined a second time using a lower peak fluence of 5.8 J/cm<sup>2</sup> and line overlap of 70% to produce the typical porous nanostructure which results from ultrafast laser micromachining of polymers [17] and supports the superhydrophobic wetting properties of the sample surfaces, as reported by Liang et al. (2014) [18]. The dimensions and properties of all 5 sample surfaces are outlined in **Table 1**.

**Table 1.** Characterization of different sample surfaces.

Surface	Nano	Wavy	H200	P100	P200
Width (W)	N/A	N/A	101.6 $\mu\text{m}$	102.8 $\mu\text{m}$	103.7 $\mu\text{m}$
Spacing (S)	N/A	10.8	198.5 $\mu\text{m}$	97.2 $\mu\text{m}$	196.3 $\mu\text{m}$
Height (H)	N/A	2.8 $\mu\text{m}$	228.5 $\mu\text{m}$	192.6 $\mu\text{m}$	236.3 $\mu\text{m}$
$\theta_A$	$165 \pm 2^\circ$	$161 \pm 5^\circ$	$165 \pm 8^\circ$	$163 \pm 5^\circ$	$163 \pm 4^\circ$
$\theta_R$	$159 \pm 7^\circ$	$153 \pm 6^\circ$	$155 \pm 5^\circ$	$156 \pm 6^\circ$	$142 \pm 5^\circ$
CAH	$6^\circ$	$8^\circ$	$10^\circ$	$7^\circ$	$21^\circ$

As shown in **Figure 1(a-b)**, the profile of the sample surfaces was imaged through scanning electron microscopy (FEI Inspect F50), along with images from a laser scanning confocal microscope (LEXT OLS4100), which conveys the topographical shape of each microstructure using a heat map. The Wavy, H200, P100, and P200 samples are hierarchical, having a microstructure that is in turn covered with a porous, wiry nanostructure. In our sample naming convention (for the P100, P200, and H200 samples), the numbers identify the spacing (S) between topographical peaks (i.e. the pore size), while P indicates a pillared microstructure and H indicates a hole microstructure. While the spacing was varied, the feature width (W) of these three samples was maintained at approximately 100  $\mu\text{m}$  (**Table 1**). However, the Wavy sample has a crest-and-trough microstructure with much smaller dimensions than the other hierarchical structures. The Nano sample has no microstructure at all and is textured only with the nanostructure that also covers the other samples.

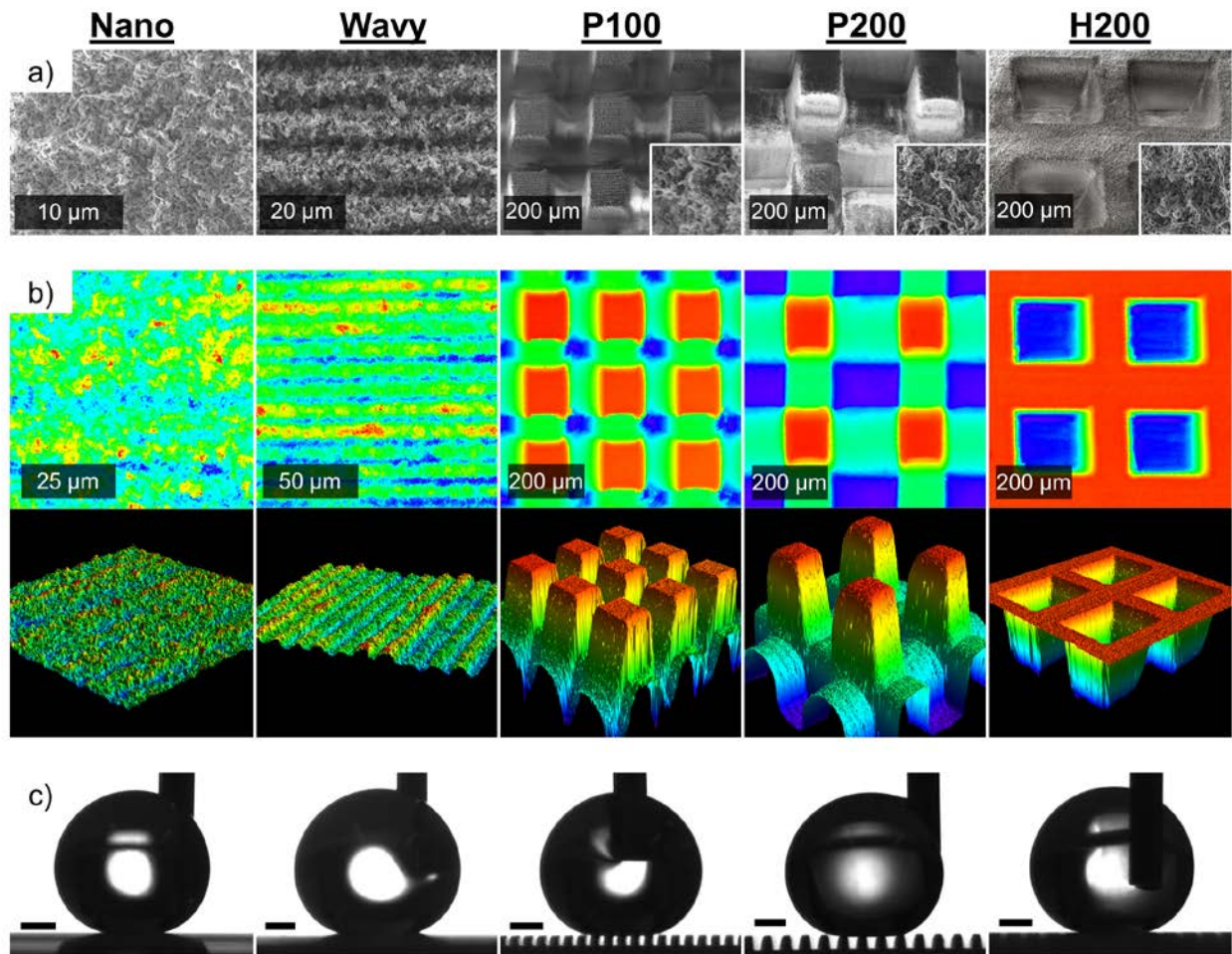


**Figure 1.** (a) SEM micrographs of the sample surfaces. The insets of the P100, P200, and H200 SEM images show a 10 μm wide zoomed view of the nanostructure. (b) Confocal microscope heat maps, along with 3D interpretations of the sample surfaces' topography. (c) Images of an advancing water drop on each sample surface during dynamic contact angle measurement. The scale bar in the corner of each image has a width of 500 μm.

For drop impact experiments, the surfaces were attached to a sample holder with an adjustable tilt angle. Water drops with a diameter of  $2.04 \pm 0.08$  mm were generated using a syringe placed above the sample, with a gauge 32 (0.24 mm outer diameter) stainless steel dispense tip, and the drop's falling velocity was controlled by changing the height from which it fell. Drop

impact experiments were performed at five discrete normal Weber numbers ( $We_n = 3.5 \pm 0.9$ ,  $9.5 \pm 1.3$ ,  $24.2 \pm 1.5$ ,  $44.9 \pm 4.3$ , and  $78.3 \pm 4.1$ ) and four different angles of incidence ( $AOI = 0^\circ$ ,  $30^\circ$ ,  $45^\circ$ , and  $60^\circ$ ), so that 20 different conditions were recorded for each surface. Each experimental condition was performed four times to confirm repeatability. Note that, for simplicity, throughout this report we will refer to the rounded average of  $We_n$ , for example  $We_n = 45$  instead of  $44.9 \pm 4.3$ . Drop impact events were recorded using a Photron FastCam SA5 high-speed camera, filming at 10,000 frames per second. The camera viewed the events through an 18–108 mm Navitar Macro Zoom 7000 lens, and backlighting was supplied using an AI SL185-WHI-IC ultra-bright spotlight (Optikon Corp.).

Using the high-speed videos,  $D_{max}^*$ ,  $\varepsilon_n$ , and  $\varepsilon_t$  were measured using custom MATLAB codes that track the shape and position of the drops throughout the impact and rebound process. In the case of impacts that fractured into two or more drop fragments after rebounding, the restitution coefficient was measured by estimating the mass of each drop fragment and tracking the center of mass of the liquid as it moves away from the surface. The codes are available through the following reference, along with demonstrative figures and examples of their application [19]. Curve fitting of **Equation 7** and **Equation 8**, as well as determination of 95% confidence intervals for the fitting factors, was accomplished using the NonLinearModel function in Matlab.

Measurements of the advancing ( $\theta_A$ ) and receding ( $\theta_R$ ) contact angles of each sample surface are stated in **Table 1**, and were performed using a Data Physics OCA 15E goniometer. For these measurements, a drop with an initial volume of 2  $\mu\text{L}$  was placed gently onto the sample surface. The volume was then increased to 12  $\mu\text{L}$  at a rate of 0.1  $\mu\text{L/s}$ , and then reduced back down to 2  $\mu\text{L}$ . An image of a water drop during the advancing stage of the procedure is shown for each surface in **Figure 1(c)**.

Immersion confocal microscopy images of the air-water interface were obtained using a Zeiss LSM880-Intravital microscope operating in reflection mode, with a 20X Plan-Apochromat dipping lens. In order to image this sample without causing a pressure buildup of the air within the superhydrophobic surface's microstructure, we designed a special sample holder to allow air to enter and leave the microstructure freely and equilibrate with the surrounding environment. Details of this custom sample holder are provided in Supporting Note 1.

## RESULTS & DISCUSSION

### OBSERVED IMPACT BEHAVIOURS

**Figure 2** shows high speed video snapshots of the different impact behaviours observed in our experiments. The original videos are available online as **Supporting Videos 1-5**. The vast majority of our experiments resulted in complete rebounding behaviour, which is shown in **Figure 2(a)** for a normal impact (a complete map of the impact behaviour on each surface is available in Supporting Note 2). The expansion phase begins immediately when the drop contacts the surface, at dimensionless time  $t^* = 0$ . As the drop deforms against the surface it slows down, and its initial kinetic energy is transferred into surface energy as the drop spreads and its surface area increases. Once the drop's kinetic energy has been completely expended and the liquid reaches its maximum spreading diameter, the retraction phase begins ( $t^* = 0.76$ ). Surface tension pulls the liquid back towards the drop's center, and surface energy is transferred back into kinetic energy as the drop thickens again and the liquid pushes off the surface and accelerates upwards [15]. Finally, in the rebound phase ( $t^* > 2.90$ ), the drop detaches from the surface and moves away entirely.

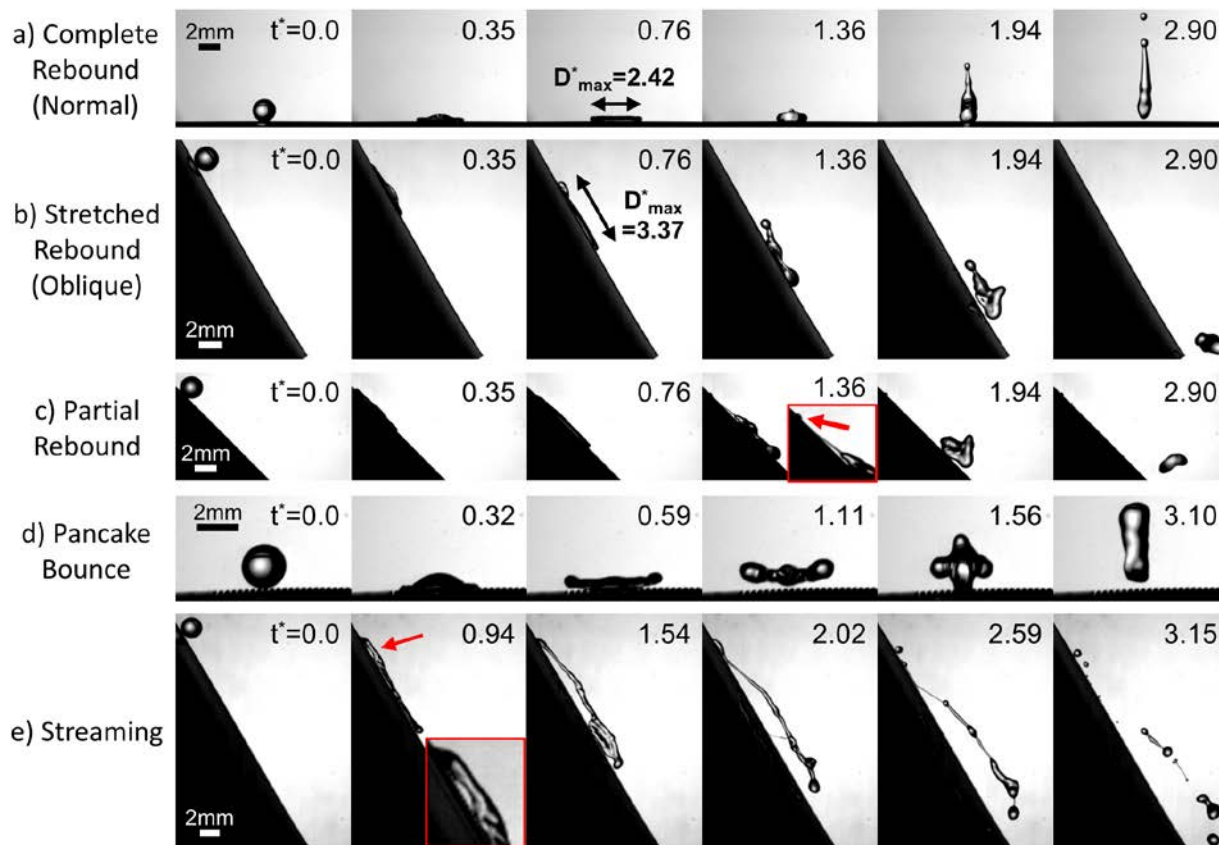


**Figure 2.** Observed impact behaviours. Exact conditions: (a) H200,  $We_n = 43.6$ ,  $AOI = 0^\circ$ . (b) H200,  $We_n = 47.1$ ,  $AOI = 60^\circ$ . (c) Wavy,  $We_n = 81.1$ ,  $AOI = 45^\circ$ . The inset shows a zoomed view of the thin strand of liquid formed, and the red arrow indicates the pinned drop at the impact center. (d) P200,  $We_n = 47.5$ ,  $AOI = 0^\circ$ . (e) P100,  $We_n = 78.2$ ,  $AOI = 60^\circ$ . The inset image shows a bridge of early liquid detachment.

**Figure 2(b)** highlights another form of complete rebounding behaviour that can occur in oblique impacts, called stretched rebounding. The sequence of events is similar to those in **Figure 2(a)**, except that due to the oblique nature of the impact, the lamella spreads into an elliptical shape (when viewed from above). This elliptical shape prompts the liquid to retract very quickly along the minor axis, causing the drop to detach from the surface quite early, at a dimensionless time of

only  $t^* = 1.94$  [16]. This mechanism will be analyzed and explained in greater detail later in this report, in the contact time section.

**Figure 2(c)** shows partial rebounding, where part of the liquid becomes pinned to the initial impact center due to the Cassie-to-Wenzel wetting transition. As the liquid bulk moves away along the surface, a thin strand of liquid keeps it connected to the pinned drop (inset,  $t^* = 1.36$ ). Finally, the main drop detaches and rebounds from the surface, and a small secondary drop is left behind at the location where the drop first contacted the surface.

**Figure 2(d)** shows pancake bouncing, which we observed only on the P200 surface. The liquid initially penetrates the surface's microstructure but is quickly ejected due to the antiwetting pressure of the air-liquid interface between the microscale pillars. Hence, the outermost perimeter of the lamella can be seen detaching from the surface as early as  $t^* = 0.59$ , and the entire drop detaches at  $t^* = 1.11$ , at which point the lamella is still very wide and has not yet retracted.

Finally, **Figure 2(e)** displays a new behaviour that we call streaming. This impact behaviour is essentially a combination of the partial rebounding and pancake bouncing behaviours, which occurred only on the P100 surface. As shown in the snapshots, while some of the liquid remains pinned to the surface at the impact center, the liquid bulk spreads tangentially down the surface, but is quickly repelled by the antiwetting pressure of the pillared microstructure. Hence, as early as  $t^* = 0.94$ , the drop begins detaching from the surface and eventually forms a long, elongated column of water moving downstream ( $t^* = 2.02$ ). Detachment finally occurs at  $t^* = 2.59$ , at which point the liquid column fractures into several small drops.

## RESTITUTION COEFFICIENT

The restitution coefficient is the ratio between the initial and final velocities of the drop during impact with the superhydrophobic surface ( $\varepsilon = v_2/v_1$ ). For oblique impacts,  $\varepsilon$  is best characterized by using the impact's angle of incidence (*AOI*) to decouple the impact velocity into its normal ( $v_n$ ) and tangential ( $v_t$ ) components (illustrated in **Figure 3(a)**). Accordingly,  $\varepsilon$  can also be decoupled into the normal restitution coefficient ( $\varepsilon_n = v_{n2}/v_{n1}$ ) and the tangential restitution coefficient ( $\varepsilon_t = v_{t2}/v_{t1}$ ). In a previous report, we measured  $\varepsilon_n$  and  $\varepsilon_t$  for oblique drop rebounds on a superhydrophobic surface, and found that both quantities are governed primarily by  $We_n$ , and can be modeled using power laws of the form:

$$\varepsilon_x = y \cdot We_n^z \quad \text{Equation 2}$$

where  $x$  denotes either the normal or tangential component, and  $y$  and  $z$  are fitting factors.

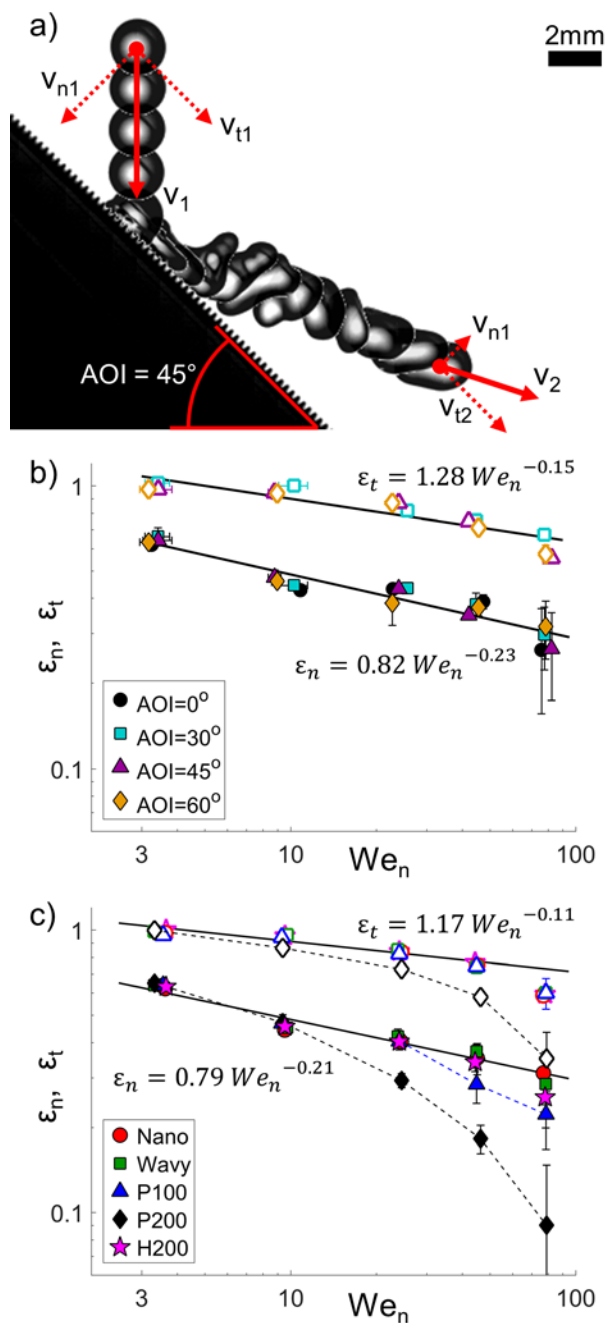


**Figure 3.** (a) Compound image of an oblique drop impact (P200 surface,  $We_n = 9.3$ ,  $AOI = 44.9^\circ$ ). The arrows indicate the initial ( $v_1$ ) and final ( $v_2$ ) drop velocity, as well as their normal and tangential components. (b) Normal and tangential restitution coefficients versus the normal Weber number for the wavy surface. Open markers indicate  $\epsilon_t$ , and closed markers indicate  $\epsilon_n$ . The values of  $\epsilon_n$  and  $\epsilon_t$  are consistent for each AOI. Equivalent plots are provided for the other 4 experimental

surfaces in Supporting Note 3. (c) Measurements of  $\varepsilon$  for all surfaces. Each data point is the average  $\varepsilon$  for each AOI tested.

The efficacy of **Equation 2** is demonstrated in **Figure 3(b)**, which plots  $\varepsilon_n$  and  $\varepsilon_t$  for the Wavy surface, at each  $We_n$  and  $AOI$  tested. Curve fitting indicates that  $\varepsilon_n = 0.82 \cdot We_n^{-0.23}$  and  $\varepsilon_t = 1.28 \cdot We_n^{-0.15}$ , which provides a good fit for the data. It is notable that, despite the oblique nature of the drop impact experiments tested, both  $\varepsilon_n$  and  $\varepsilon_t$  show no dependence on the  $AOI$  but are instead governed entirely by  $We_n$ .

Furthermore,  $\varepsilon_t$  is significantly higher than  $\varepsilon_n$  across the entire experimental range (**Figure 3(b)**). Accordingly, after rebounding, oblique drop impacts usually retain most of their velocity in the tangential direction but suffer significant energy losses to the normal velocity. To explain this discrepancy, we consider the different mechanisms that govern the restitution coefficient in the normal and tangential dimensions. For the normal dimension, some energy is lost to viscous dissipation during the expansion phase of impact, while the drop's initial kinetic energy is being transferred into surface energy. Then, during retraction, more energy is lost into vibrational modes as the liquid recombines and bounces off the surface. These two factors have been identified as the governing factors of  $\varepsilon_n$  [6, 15, 20]. However, since  $\varepsilon_t$  is a more recently introduced concept, the governing factors are not yet certain. In a previous report, we hypothesized that  $\varepsilon_t$  is governed by adhesion, such that the tangential sliding motion of the drop is hindered by points of solid-liquid contact between the liquid and solid surface [15].

This hypothesis can be tested by comparing the restitution coefficients of all 5 different microstructures tested in this report, as shown in **Figure 3(c)**. Four of the surfaces (Nano, Wavy, H200, and P100) follow a common trend, as shown by the solid black lines. However, the

restitution coefficient of the P200 surface diverges significantly. We will first discuss the trends of the four surfaces that follow the model lines, and then move on to the unique case of the P200 surface.

There are significant differences between the structures of the Nano, Wavy, H200, and P100 samples. For example, the H200 sample represents the only closed-cell microstructure. The Wavy microstructure has feature spacing of only  $S = 10 \mu\text{m}$ , as opposed to  $S = 100 \mu\text{m}$  and  $S = 200 \mu\text{m}$  for the P100 and H200 surfaces, respectively. And the Nano sample only has a nanoscale topography, as opposed to the hierarchical micro/nanoscale structures of the other samples. However, despite all of these significant differences in morphology, **Figure 3(c)** shows that both  $\varepsilon_n$  and  $\varepsilon_t$  stayed remarkably consistent as the microstructure was varied. In the range of  $3 \leq We_n \leq 44$ , the restitution coefficients of the oblique impacts tested can be accurately modeled by the following power laws:

$$\varepsilon_n = 0.79 \cdot We_n^{-0.21} \quad \text{Equation 3}$$

$$\varepsilon_t = 1.17 \cdot We_n^{-0.11} \quad \text{Equation 4}$$

The fact that **Equation 3** and **Equation 4** match most of the data in **Figure 3(c)** indicates that, in general, the microstructure of a superhydrophobic surface has little to no influence on the restitution coefficient.

However, starting at  $We_n = 78$ , the values of  $\varepsilon$  for every surface drop below the trend line. This occurs because, at this high Weber number, drop pinning occurred on each experimental surface, resulting in partial rebounding or streaming behaviour instead of complete rebounding. This shift from complete rebounding behaviour to pinning can be visualized by comparing **Figure 2(a-b)** ( $We_n = 44$ ) with **Figure 2 (c)** ( $We_n = 78$ ). The value of  $\varepsilon$  decreases when drop pinning occurs because the attachment of the drop to the surface causes the liquid to stretch, increasing the

overall area of the liquid-air interface. This phenomenon is clearly visible in **Figure 2(c)**, where the presence of pinning results in the formation of a thin strand of liquid that tethers the drop's tail to the surface ( $t^* = 1.36$ ). The creation of this added surface area requires energy, which must be subtracted from the drop's kinetic energy during the rebound process. Further, when the liquid tether disconnects, more energy is lost into vibrational modes as the outstretched liquid is drawn back towards its center and continues to oscillate ( $t^* = 1.94$ ). These energy losses related to liquid pinning explain why, at  $We_n = 78$ , both  $\varepsilon_n$  and  $\varepsilon_t$  drop below the trend line in **Figure 3(c)** for every surface tested.

Now, regarding P200, the restitution coefficient of this sample diverges significantly from all the other surfaces due to the presence of pancake bouncing behaviour. As explained in the introduction, pancake bouncing causes drops to detach extremely early from the surface due to capillary ejection of the liquid intruding between the micro-pillars. Hence, as shown in **Figure 2(d)**, drops impacting the P200 surface can detach at dimensionless times as early as  $t^* = 1.02$ . In our experiments, we observed pancake bouncing on the P200 surface for impacts at  $We_n \geq 24$ , which is exactly where the restitution coefficient begins to decline. We suggest that pancake bouncing reduces  $\varepsilon_n$  because in most rebounding drop impacts, the drop regains momentum in the normal direction while the liquid retracts back towards the liquid bulk, which increases the thickness of the drop and pushes it off the surface (see **Figure 2(a)**). However, in the case of pancake bouncing, the drop detaches from the surface while still fully outstretched, without retracting and growing thicker. The consequence of this mechanism is that the kinetic energy of the drop as it rebounds is gained mainly from the capillary ejection mechanism, which exerts less lifting pressure ( $P_{lift}$ ) on the drop than the conventional retraction mechanism that occurs for most superhydrophobic surfaces.

This assertion can be quantified by comparing a pressure balance of the retraction mechanism with that of the pancake bouncing mechanism. At the start of the retraction phase, the drop has a normal velocity of  $v_n = 0$ , and then accelerates its normal velocity up to  $v_{n2}$  while increasing in thickness and pressing off of the surface. Since the retraction time is proportional to the inertial-capillary time ( $t_{retr} \propto \sqrt{\rho D_0^3 / \sigma}$ ), the acceleration during this phase is proportional to  $a_{retr} \propto v_{n2} / \sqrt{\rho D_0^3 / \sigma}$  [11]. Next, the definition of the normal restitution coefficient states that  $v_{n2} = \varepsilon_n v_{n1}$ . And from **Equation 3**, we know that  $\varepsilon_n \propto We_n^{-0.21}$  which, considering the definition of  $We_n$ , leads to  $\varepsilon_n \propto v_{n1}^{-0.42}$ . Substituting these equations, we find that the acceleration can be stated as  $a_{retr} \propto v_{n1}^{0.58} / \sqrt{\rho D_0^3 / \sigma}$ . Then, from Newton's second law of motion, the lifting force on the drop during the retraction process ( $F_{lift,retr}$ ) is proportional to the product of the drop's mass ( $m \propto \rho D_0^3$ ) and acceleration ( $a_{retr}$ ), so that  $F_{lift,retr} \propto v_{n1}^{0.58} \sqrt{\rho D_0^3 \sigma}$ . Finally, dividing this force by the area ( $A \propto D_0^2$ ), we find the lifting pressure on a rebounding drop during the conventional retraction mechanism:

$$P_{lift,retr} = k \cdot v_{n1}^{0.58} \sqrt{\rho \sigma / D_0} \quad \text{Equation 5}$$

where  $k$  is a constant. The value of  $k$  can be estimated by fitting this equation to the experimental results of Lee et al. (2015), who analyzed the threshold impact velocity for pinning on 6 different superhydrophobic microstructures [11]. This method produces a value of  $k \approx 4.5$  (full analysis can be found in Supporting Note 4). Accordingly, over the range of Weber numbers tested in this report, we estimate that the lifting pressure via the retraction mechanism ranges from approximately  $P_{lift,retr} \approx 500$  to 1100 Pa.

In contrast, the lifting pressure of pancake bouncing ( $P_{lift,pan}$ ) depends entirely on the anti-wetting pressure of the air-liquid interface that bends down in between the peaks of the pillared microstructure. A unit cell of the P200's square pillar microstructure has a width of  $W + S$ , where  $W$  is the width of the pillar and  $S$  is the spacing between adjacent pillars. The antiwetting force is given by the product of the vertical component of the surface tension,  $\sigma \cos \theta_A$ , and the perimeter of single pillar,  $4W$ . This force acts over an area equal to that of the unit cell  $(W + S)^2$  minus the area of the pillar itself ( $W^2$ ). Therefore, dividing the force by the area of the cavity, for pancake bouncing the maximum lifting pressure is given by:

$$P_{lift,pan} = \frac{4W\sigma \cos \theta_A}{(W + S)^2 - W^2} \quad \text{Equation 6}$$

To calculate an actual value of  $P_{lift,pan}$ , we use the approximate measurements of  $W \approx 100 \mu\text{m}$  and  $S \approx 200 \mu\text{m}$  for P200 (see **Table 1**). Then, since the surface is covered with the same nanostructure that is present on the entire Nano sample, we can use our measurement of  $\theta_A = 165^\circ$  from that sample. Hence, the estimated maximum lifting pressure for pancake bouncing is  $P_{lift,pan} = 347 \text{ Pa}$ , which is significantly lower than the lifting pressure of the retraction mechanism of rebound. This pressure balance confirms that  $\varepsilon_n$  on the P200 surface is especially low because the pancake bouncing mechanism applies less lifting pressure on the drop than the conventional retraction mechanism that occurs on most superhydrophobic surfaces.

To summarize the above discussion, surfaces with sparsely spaced posts, which can trigger the pancake bouncing mechanism, have a unique influence on the restitution coefficient of rebounding drops. However, for most superhydrophobic surfaces, the microstructure has little to no influence on either  $\varepsilon_n$  or  $\varepsilon_t$ . For the case of the normal restitution coefficient, this lack of dependence between  $\varepsilon_n$  and the surface topography was expected, since  $\varepsilon_n$  is governed by energy

losses during the expansion and retraction phases of impact, which is not greatly affected by variations in microstructure. This explains why **Equation 3** is consistent with a correlation published by Aria et al., who measured  $\varepsilon_n$  on a superhydrophobic carbon nanotube nanoforest, and found that  $\varepsilon_n = 1.1 We_n^{-0.25}$ . However, it is very surprising that  $\varepsilon_t$  shows no dependence on the surface topography since, as we will show in the next section, the adhesion present between the drop and superhydrophobic surface is highly dependent on the microstructure. Unfortunately, this discrepancy sheds doubt on our earlier theory that  $\varepsilon_t$  is governed mainly by friction. And we are not aware of any other articles reporting values of  $\varepsilon_t$  on a superhydrophobic surface that we can compare our results to. Hence, we suggest that future research focuses on measuring  $\varepsilon_t$  on superhydrophobic surfaces that are composed of a variety of different materials and have different nanostructures, in order to isolate other possible variables that might influence the value of  $\varepsilon_t$ , and better understand the principles that govern oblique drop rebounding.

## MAXIMUM SPREADING DIAMETER

To model the spreading behaviour of oblique drop impacts, we begin by characterizing the dimensionless maximum spreading diameter of normal drop impacts ( $D_{n,max}^*$ ), and then expand on that model for the oblique case. **Figure 4** plots  $D_{n,max}^*$  versus  $We_n$  for all 5 sample surfaces. The dashed line indicates a model fit using **Equation 1**, with  $D_{n,max}^* = 0.74 \cdot We_n^{0.30}$ . This model agrees well with the data for  $We_n \geq 10$ , but fails to capture  $D_{n,max}^*$  for low Weber numbers. This occurs because **Equation 1** predicts that as  $We_n$  approaches zero, so does  $D_{n,max}^*$ . However, even a drop that is placed gently on a superhydrophobic surface (with  $v_n = 0$  and  $We_n = 0$ ) has a tangible footprint, and thus a non-zero  $D_{n,max}^*$ . Hence, it is obvious that **Equation 1** will always fail at low Weber numbers.

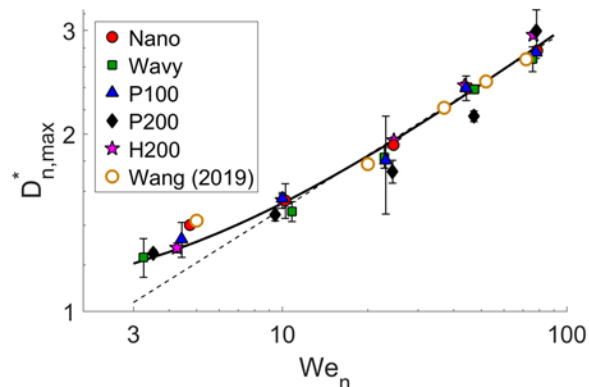


**Figure 4.** Maximum spreading diameter of impacts at normal angle of incidence for all 5 experimental samples. The dashed line shows a fit using **Equation 1**, and the solid line using **Equation 7**.

This problem can be rectified by altering **Equation 1** into the following form, which does not approach zero at low Weber numbers:

$$D_{n,max}^* = (aWe_n + 1)^b \quad \text{Equation 7}$$

The solid black line in **Figure 4** shows **Equation 7** after model fitting is performed, which results in values of  $a = 0.24$  and  $b = 0.35$ . The model gives an excellent fit for  $D_{n,max}^*$  across the entire range of Weber numbers. Also included in the plot are measurements by Wang et al. (2019), who measured  $D_{n,max}^*$  for impacts ranging from  $5 \leq We_n \leq 72$  on a nanostructured superhydrophobic surface coated in trichloro-(1H,1H,2H,2H-perfluorooctyl)silane. Their measurements are also well predicted by **Equation 7**, which demonstrates that this simple empirical model is applicable to superhydrophobic surfaces beyond this study.

Modeling the oblique maximum spreading diameter ( $D_{max}^*$ ) is more complex than the case of normal impact. While the drop slides tangentially across the superhydrophobic surface during the expansion and retraction phases, it experiences some adhesion to the surface, caused by sites of solid-liquid contact. This adhesion acts to stretch the drop, causing its maximum spreading

diameter to increase. Based on this stretching mechanism, in a previous report we derived a model for  $D_{max}^*$  that is a function of  $D_{n,max}^*$ , the  $AOI$ , and  $We_n$  [14]. For this report, we have refined the model by emphasizing the dynamic pressure of impact ( $P_d = \rho v_{n1}^2$ ) rather than  $We_n$ , which led to **Equation 8**. For the sake of brevity, the complete derivation of this model, along with an explanation of the differences to the previous version, is available in Supporting Note 5.

$$D_{max}^* = D_{n,max}^* + c \cdot \tan(AOI) \sqrt{We_n} (\rho v_{n1}^2) \quad \text{Equation 8}$$

This model essentially states that the oblique spreading diameter is equal to the expected spreading diameter for a normal impact ( $D_{n,max}^*$ ) plus a second term which we call the stretching length, that accounts for the stretching mechanism described above. The variable  $c$  is the adhesion coefficient, and quantifies the adhesive properties of the superhydrophobic surface [14].

**Figure 5(a-e)** plots  $D_{max}^*$  for all 5 surfaces, along with the model fits from **Equation 8**. The influence of different microstructures on  $D_{max}^*$  can be quantified using the values of the adhesion coefficient ( $c$ ) obtained from the different model fits, which is stated for each surface on their respective plots in **Figure 5(a-e)**. Higher values of  $c$  indicate greater adhesion between the drop and sample, which leads to an increase in  $D_{max}^*$  as the drop slides tangentially across the surface. In our experiments, we found the lowest value of  $c = 1.20 \times 10^{-5}$  for the Nano surface, indicating very low drop adhesion on that sample. Conversely, the value of  $c = 3.23 \times 10^{-5}$  for H200 is more than twice as high, as is evident from the high slopes of the model lines for H200 in **Figure 5(c)**.

The model performs well for the majority of our experiments, and accurately matches the data points. However, we found that the model is not suited to describing the spreading behaviour of impacts that exhibit pinning behaviour. The experimental settings where pinning occurred are indicated in the figure by the open markers. These points were excluded from model fitting since

the derivation of **Equation 8** assumes that the liquid drop is slowed by adhesion forces, but is not completely pinned to the surface (the importance of this distinction can be understood by comparing **Figure 2(a)**, which shows complete rebounding, with **Figure 2(c)**, where drop pinning results in partial rebounding). Since drop pinning causes the tail of the drop to remain stuck at the initial impact center, the value of  $D_{max}^*$  reaches exceedingly high values as the front of the drop continues to slide along the surface, stretching the drop's length. Thus, for the sake of quantitative analysis, we will ignore the open markers, where pinning occurred. Furthermore, model fitting was not successful for the P200 surface. This is because, much like the restitution coefficient,  $D_{max}^*$  is significantly affected by pancake bouncing. On the P200 surface, we observed various combinations of pinning, very early detachment ( $t_c^* \approx 1$ ), streaming, and in some cases splashing. This combination of different behaviours has so far led to unpredictable values of  $D_{max}^*$ . As a result, model fitting resulted in a negative value of  $c$ , which is not scientifically meaningful or useful for quantitative prediction. Therefore, we consider **Equation 8** to be unsuccessful for predicting  $D_{max}^*$  for our P200 surface, and i.e. for pancake bouncing drops and also pinning drops in general.

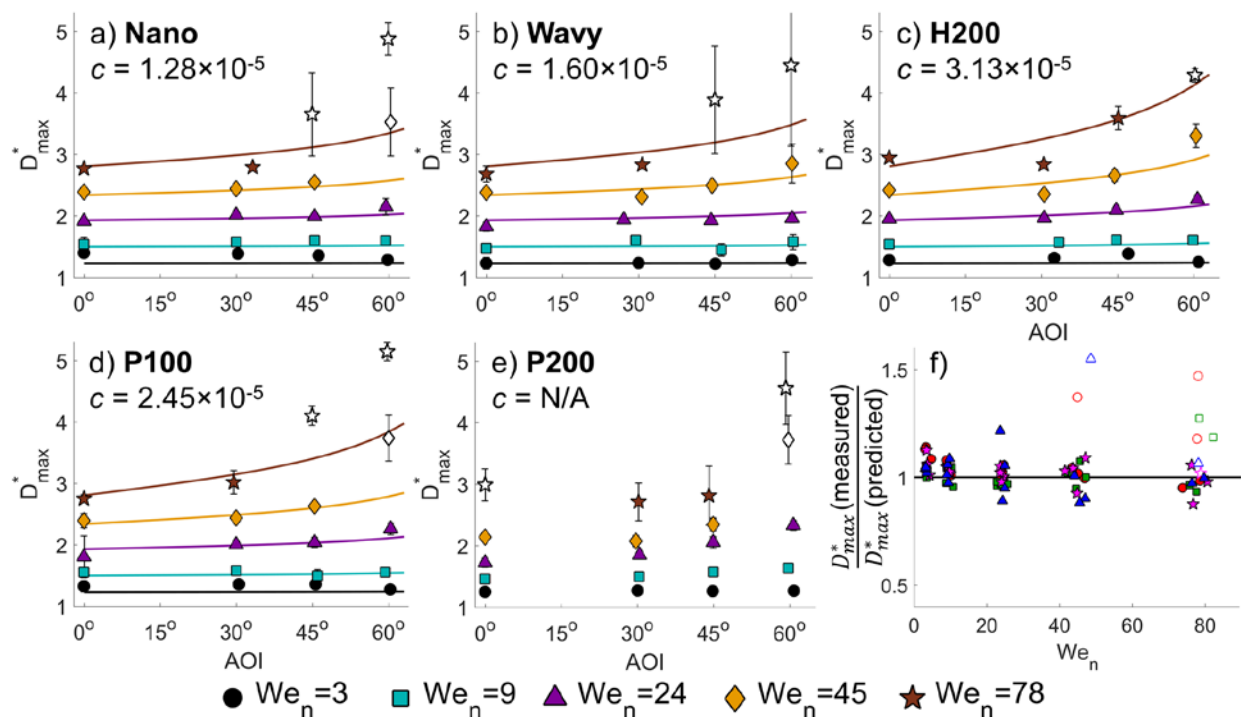


**Figure 5.** (a-e) Model fits of **Equation 8** for each microstructure. Open markers indicate experiments where drop pinning occurred. (f) Comparison between the measured values of  $D_{max}^*$  and those predicted by **Equation 8**. The open symbols indicate experiments where significant drop pinning occurred. Error bars are excluded for clarity.

Despite these discrepancies, for the majority of our experiments that exhibited complete rebounding behaviour, **Equation 8** is successful in modeling  $D_{max}^*$ . This can be assessed broadly through **Figure 5(f)**, which plots the ratio of the measured values to those predicted by the model, such that values near unity indicate good agreement between measurement and model. All of the solid markers (which indicate complete rebounding drops) lie close to unity, with an average error of only 4.7%. For comparison, we have again included open markers, showing experiments where pinning occurred, and for which **Equation 8** fails to accurately model  $D_{max}^*$ .

In order to make **Equation 8** useful as a predictive model,  $c$  must be correlated with the physical properties of the superhydrophobic surface. To this end, we have found that  $c$  correlates well with the overall surface area of the different superhydrophobic microstructures, which we have characterized in terms of the *microstructure roughness* ( $R_m$ ). We define  $R_m$  as the ratio of the total surface area of the topographical microstructure, as compared to its area as seen from a “bird’s eye view” (i.e. a flat surface). Note that since we are presently only interested in the shape of the microstructure geometries, we ignored the nanostructure that is superimposed on each structure. Therefore, it should be noted that  $R_m$  is different than the roughness ratio ( $R$ ) defined by Wenzel’s wetting model, which characterizes the total surface area of both the micro- and nanostructure of the surface [21]. Accordingly, since the Nano surface has only a nanostructure and no microstructure, it is considered to be flat for the sake of this analysis, with a microstructure roughness of  $R_m = 1.0$ . In contrast, the P100 sample has a much higher value of  $R_m = 2.79$  due to the presence of micro-scale pillars. The values of  $c$  and  $R_m$  for all 5 sample surfaces are available in **Table 2**, and their correlation is plotted in **Figure 6(a)**, showing a clear, positive trend. This indicates that microstructures with greater  $R_m$  lead to more solid-liquid adhesion during sliding. Hence, it is clear that the spreading diameter of oblique drop impacts is greater on surfaces with more overall surface area.

**Table 2.** Values of the adhesion coefficient and microstructure roughness for each experimental surface.

Surface	Nano	Wavy	H200	P100	P200
$c$ [ $10^{-5}$ ]	1.28	1.60	3.13	2.45	N/A
	$\pm 0.97$	$\pm 0.70$	$\pm 0.80$	$\pm 0.94$	
$R_m$	1.00	1.03	2.69	2.79	3.85

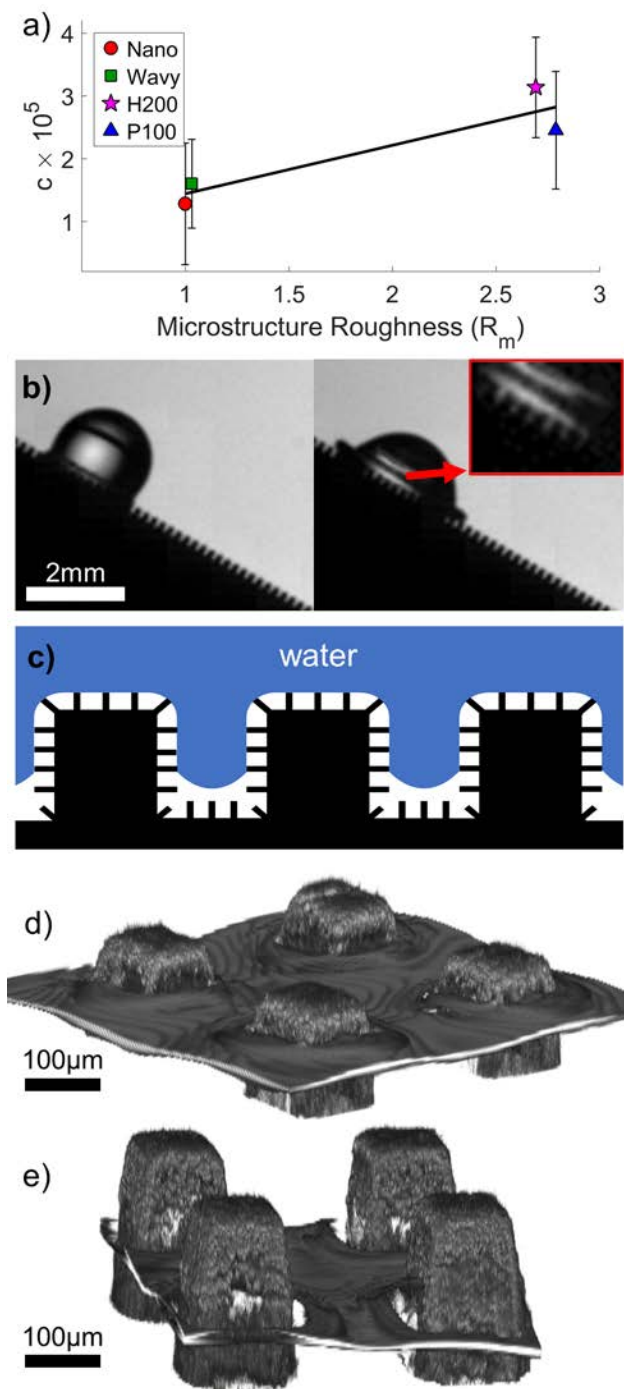


**Figure 6.** (a) Adhesion coefficient from Equation 8 (c) versus  $R_m$ . (b) Snapshots of a drop impact on the P100 surface ( $We_n = 46.5$ ,  $AOI = 30^\circ$ ). As emphasized by the inset image, the liquid penetrates between the microscale pillars. (c) Schematic of the liquid interface penetrating the hierarchical structure of the surface. (d-e) Immersion confocal microscopy images of the air-water

interface suspended among the tops of pillars on the P200 surface. The hydrostatic pressure in each image 248.3 Pa (d), and 300.7 Pa (e).

This correlation is easily rationalized. During the spreading phase of impact, the liquid interface penetrates the pores of the microstructure and forms sites of solid-liquid contact not only with the topographical peaks, but also with the sides of the microscale features, and the base of the trenches beneath them. This phenomenon is demonstrated in **Figure 6(b)**, which shows exemplary snapshots of a drop impact on the P100 surface during the start of the spreading phase. In these images, the space between successive pillars of the microstructure is clearly visible, and the liquid can be seen penetrating between the pores and filling the microstructure immediately beneath the drop. However, since the drop does not pin to the surface (aside from very high  $We_n$  cases), it can be surmised that the air pockets contained by the hierarchical nanostructure remain intact, such that the liquid makes contact only with the outermost portion of the wiry nanostructure. This wetting state is known as the rose petal effect [22], and is illustrated by **Figure 6(c)**, which offers a schematic of the liquid interface penetrating only the microscale pores of the hierarchical structure during impact. Due to this wetting state, as the drop slides tangentially away from the impact center its motion is hindered as the liquid must break its adhesion to the many different faces of the structure. **Figure 6(d-e)** further emphasize this mechanism through immersion confocal microscopy images of the P200 surface. Using this imaging technique, the liquid-air interface of the drop hanging between the pillars of the surface can be directly imaged. At both pressures tested, it is clear that the liquid interface contacts not only the topographical peaks, but also the sides of the microscale pillars, creating many additional sites of solid-liquid contact that

would not be available on a flat surface. It is this additional surface area that leads to the higher adhesion coefficient that we observe on the P100 and H200 sample surfaces.

Furthermore, the positive correlation between  $c$  and  $R_m$  is interesting because it suggests that for large, sparsely spaced microscale features (such as those on P100 and H200), the presence of a microstructure can actually lead to greater adhesion than would be present on a nanostructure-only superhydrophobic surface. This idea is somewhat counterintuitive since, typically, hierarchical structuring improves the properties of superhydrophobic surfaces. An obvious example of this is the evolved hierarchical micro/nanostructure of the lotus leaf, which promotes the self-cleaning properties that have made the species famous [4]. However, lotus leaves tested by gentle contact angle goniometry exhibit Cassie state wetting, in which both the microstructure and nanostructure remain filled with air. In contrast, on our samples, the microstructure becomes filled with water due to the dynamic pressure of impact (**Figure 6(c)**). Hence, during oblique impacts, where the drop slides tangentially across the face of the surface, the penetrating water must evacuate from the large microstructure pores and rejoin the liquid bulk as the drop slides past the original impact center. As a result, we have observed that drop impacts on the P100 and H200 surfaces, which have very rough microstructures, exhibit turbulence in the lamella while sliding. This is evidenced by Supporting Video 6 (available online), which shows four equivalent drop impacts at  $We_n = 45$  and  $AOI = 30^\circ$  occurring in synchronization on the Nano, Wavy, H200, and P100 surfaces. On the Nano surface, which has no microstructure, the lamella remains smooth and unperturbed while the drop slides tangentially across the surface. However, on the H200 and P100 surfaces, the tail of the lamella is significantly perturbed by the rough microstructure of the surface, to the point that large undulations propagate across the lamella each time the tail crosses another feature peak, causing the tail of the lamella to flutter. This fluttering phenomenon provides

additional evidence that micro-scale pores in the surface topography can create sites of adhesion during oblique impacts, which are responsible for the positive correlation between  $c$  and  $R_m$ .

In summary of this section, the spreading diameter of oblique drop impacts on superhydrophobic surfaces is governed not only by the impact speed and the AOI, but also by the adhesion coefficient of the surface, which is related to the overall surface area of the microstructure. In future studies, we suggest that materials other than PTFE should be tested, along with different nanostructures, to determine how different material characteristics, and different nanostructure geometries and patterns, influence  $c$  and  $D_{max}^*$ .

## CONTACT TIME

The dimensionless contact time ( $t_c^*$ ) spans from the first moment of contact between the drop and surface to their eventual detachment. However, impacts that result in partial rebounding or streaming behaviour leave a small secondary drop behind. For the sake of analysis, in these cases we have taken  $t_c^*$  as the time required for the liquid bulk to disconnect from the pinned segment, but it should be understood that some fraction of the liquid remains in contact with the surface indefinitely. In the following discussion we will focus first on explaining the overall trends for the Nano, Wavy, and H200 surfaces, all of which behave very similarly. Then afterwards we will consider the cases of the P100 and P200 surfaces, whose behaviour is unique.

As noted in the introduction, many published reports have found that for water drops bouncing on a flat superhydrophobic surface, the value of  $t_c^*$  remains consistent at around 2.6, regardless of the impact velocity (and therefore also the Weber number) [6, 9]. This unintuitive fact has been explained by Richard et al (2002), who compared the mechanism of a bouncing drop to that of a classic harmonic spring, for which the period of oscillation is known to be independent

of the oscillation length. In this comparison, the liquid's inertia ( $\rho D_0/t_c^2$ ) and surface tension forces ( $\sigma/D^2$ ) are analogous to the inertia and spring constant of the oscillating spring system.

Hence, balancing those two terms, one finds that  $t_c \propto \sqrt{\rho D_0^3/\sigma}$ , indicating that the contact time depends only on the size and liquid properties of the drop, but not on the impact velocity [9].

Our contact time measurements at  $AOI = 0^\circ$  (**Figure 7(a)**) are in good agreement with this theory. As  $We_n$  is raised,  $t_c^*$  exhibits on a very weak correlation with the Weber number, with a linear fit of  $t_c^* = 2.62 + 0.007 \cdot We_n$ . The value of  $t_c^*$  rises slightly at higher Weber numbers because, as has been demonstrated previously, higher impact speeds lead to increased penetration of the impacting liquid into the microstructure and nanostructure of a superhydrophobic surface [15]. Therefore higher- $We_n$  impacts result in a higher liquid-solid contact area. This leads to greater adhesion between the drop and sample, and ultimately causes drop pinning at very high  $We_n$ . As described previously, pinning behaviour generates a thread of liquid that connects the drop to the surface even while they begin to separate during the rebound phase (top-right inset of **Figure 7(a)**). Once the liquid bulk has moved sufficiently far away from the surface, the thread becomes greatly elongated and severs.

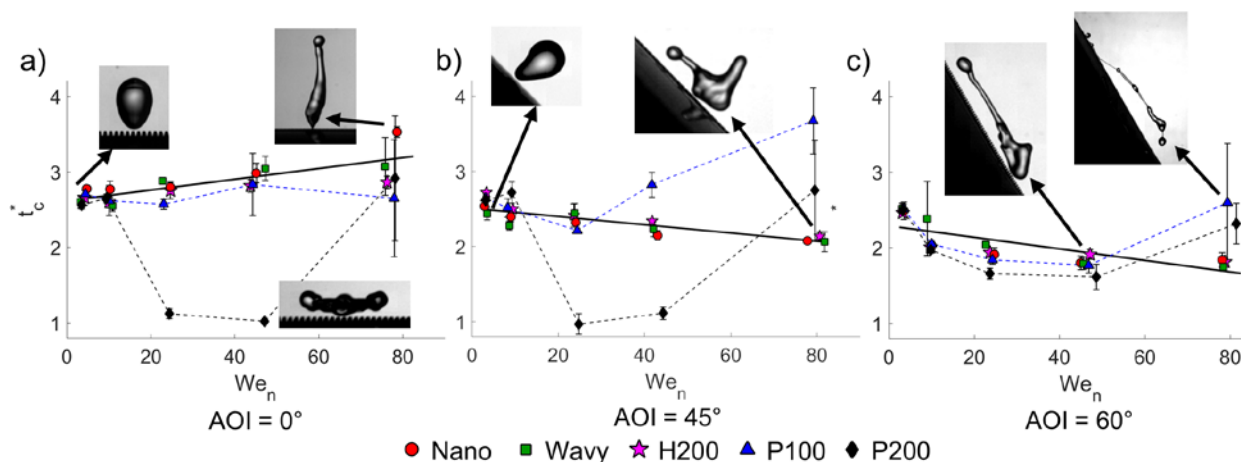


**Figure 7.** Evolution of the dimensionless contact time as  $We_n$  is raised. A plot for  $AOI = 30^\circ$  is available in Supporting Note 6 (online).

**Figure 7(b-c)** show the evolution of  $t_c^*$  for oblique impacts at  $AOI = 45^\circ$  and  $60^\circ$ . Again, the behaviour among the Nano, Wavy, and H200 surfaces is very consistent. However, where  $t_c^*$  and  $We_n$  were positively correlated at  $AOI = 0^\circ$ , we found a negative correlation in our oblique impact experiments. This is illustrated by the solid black lines in **Figure 7(b-c)**, which begin with values of  $t_c^* \approx 2.5$  at low  $We_n$ , and then decline to  $t_c^* \approx 2.0$  for high  $We_n$ . The decrease in  $t_c^*$  with increasing  $We_n$  can be explained by the presence of stretched rebounding behaviour, which is caused by the distorted shape of the lamella in oblique impacts. To explain this phenomenon, **Figure 8(a)** presents synchronized snapshots of side view and the above view of a drop exhibiting stretched rebounding, and **Figure 8(b)** plots the drop's dimensionless spreading diameter in both the tangential and lateral directions. Due to the drop's sliding motion, the maximum spreading diameter in the tangential direction ( $D_{max}^*$ ) reaches much greater values than the maximum spreading diameter in the lateral direction ( $D_{lat,max}^*$ ), by a factor of about 1.5. In fact, as shown by the red dotted line in **Figure 8(b)**, the liquid spreading in the lateral direction remains almost exactly equal to the diameter of a drop impacting normally on a flat surface, which is also plotted in **Figure 8(b)** for comparison (red dotted line). Accordingly, during oblique impacts, the lamella deforms to an elliptical shape (as viewed from above), as can be seen in **Figure 8(a)** at  $t^* = 0.28$  to 0.67. This elliptical shape causes oblique impacts to have a greater overall surface area than normal drop impacts. As a result of this increased surface area, the force of the surface tension pulling the liquid back towards the center is increased, causing the liquid to retract much sooner than usual in the lateral direction. Hence, in **Figure 8(a-b)**, the diameter of the lamella in the lateral

direction is observed quickly retracting back towards the center ( $t^* = 1.47$ ), leading the drop to quickly detach from the surface at  $t^* = 2.14$ .

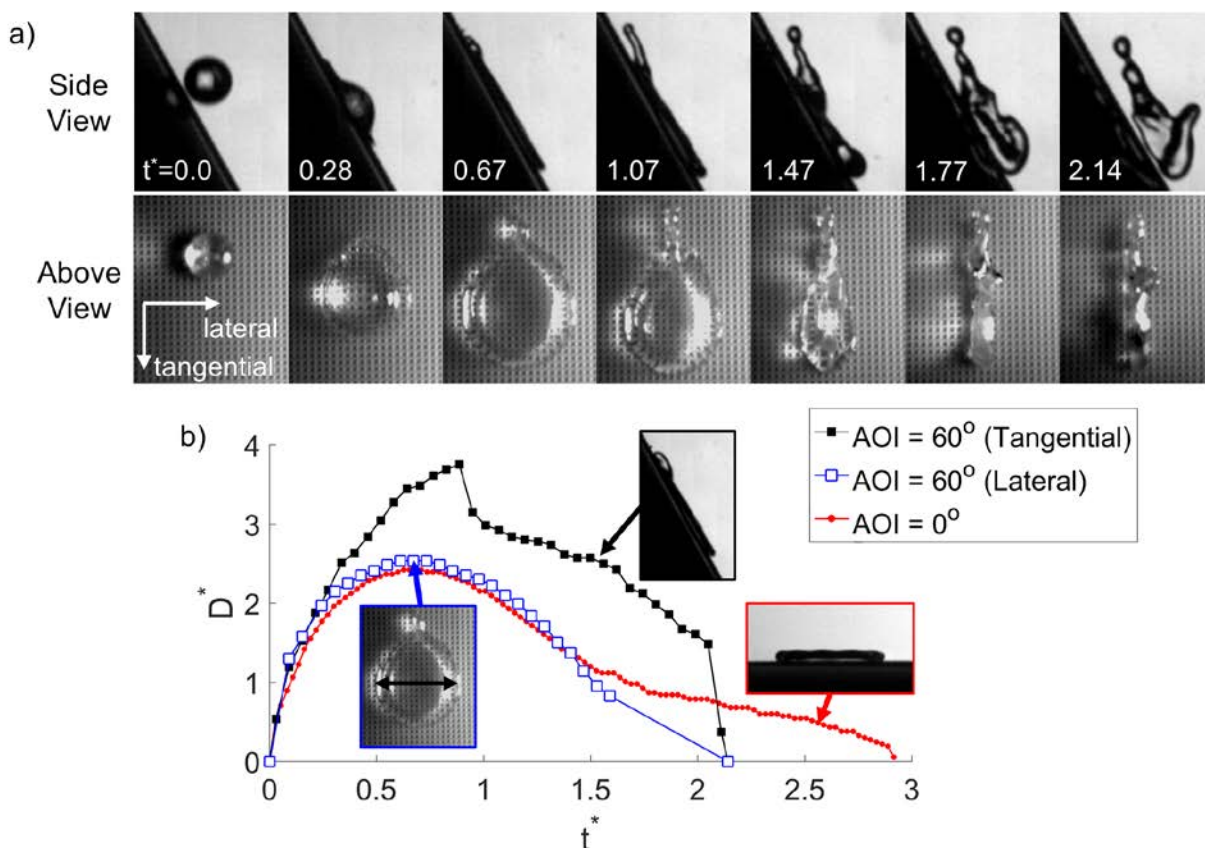


**Figure 8.** (a) Synchronized comparison of the side view and above view of a drop exhibiting stretched rebounding on the H200 surface ( $We_n = 45.0$ ,  $AOI = 60.5^\circ$ ). The original videos are viewable online (Supporting Video 8). (b) Dimensionless spreading diameter versus dimensionless time. The tangential and lateral dimensions of a stretched rebounding drop are compared to the axisymmetric spreading of a drop rebounding on a flat surface.

This early retraction mechanism is responsible for the short contact time associated with stretched rebounding behaviour. Furthermore, in **Figure 7(b-c)**, the gradual decrease in  $t_c^*$  as  $We_n$  is raised can now be explained. As demonstrated in the discussion above, the sliding motion of

oblique impacts stretches  $D_{max}^*$  in the tangential direction, and this stretching mechanism becomes more significant for impacts at higher  $We_n$  (see **Equation 8**). Meanwhile, as shown in **Figure 8(a)**, the lateral spreading of oblique impacts is unaffected by drop sliding, and always remains close to the normal spreading diameter ( $D_{lat,max}^* \cong D_{n,max}^*$ ) [14, 23, 24]. Therefore, in oblique impacts the aspect ratio between the tangential and lateral spreading diameter, which is the driving force behind the early retraction mechanism of stretched rebounding, grows monotonically as  $We_n$  increases. This relationship leads to the negative correlation between  $t_c^*$  and  $We_n$  for oblique drop impacts on superhydrophobic surfaces.

This dependence of  $t_c^*$  on the AOI also brings up an interesting discussion point. In the first section of the discussion, we established that there is a positive correlation between  $D_{max}^*$  and the AOI, and in the restitution coefficient section we established that there is no correlation between either  $\varepsilon_n$  or  $\varepsilon_t$  and the AOI. And here we have shown a negative correlation for the contact time. The reason that each of these characterizations has a different relationship with the AOI is because they all have different governing mechanisms.  $D_{max}^*$  is governed by adhesion forces acting to stretch the drop during sliding.  $t_c^*$  is governed by the early retraction mechanism described above.  $\varepsilon_n$  is governed by viscous dissipation and energy losses into vibrational modes. And it is not yet clear what factors affect the magnitude of  $\varepsilon_t$ . These different mechanisms explain why we observe different relationships between the AOI and each variable measured in this report.

Now, considering the remaining sample surfaces, the evolution of  $t_c^*$  for the P200 surface is unique from the other microstructures tested. As illustrated by the dashed black lines in **Figure 7**,  $t_c^*$  for P200 drops to values as low as 1.02 at  $We_n = 24$  and  $We_n = 45$ . This sudden drop in  $t_c^*$  occurs due to the presence of pancake bouncing behaviour, which allows the drop to rebound from the surface in less than half of the usual time (bottom-right inset of **Figure 7(a)**). However,

at  $We_n = 78$ , the contact time for P200 is similar to that of the other microstructures because, at this high Weber number, the normal restitution coefficient is so low that the drop barely leaves the surface at all. As a result, while the drop oscillates in shape after the spreading phase, parts of the liquid touch back down onto the superhydrophobic surface at different times, consistently maintaining contact with the surface in various locations. This interesting behaviour is demonstrated in Supporting Video 7 (available online) for a drop impact on P200 at  $We_n = 78$  and  $AOI = 0^\circ$ .

Finally, the contact time of the P100 surface also demonstrates unique trends as  $We_n$  is raised (dashed blue lines in **Figure 7**). As illustrated by the inset in **Figure 7(c)**, this is primarily a consequence of the streaming behaviour observed for this surface. Hence, the drop starts to detach from the surface quite early but remains connected to a pinned drop by an elongated column of water (**Figure 2(e)**). Detachment finally occurs once the liquid bulk moves far enough from the surface to sever the connection, which seems to be a fairly random process, as evidenced by the relatively large error bars for P100 at high  $We_n$  in **Figure 7(a-c)**. Hence, the contact time of drops that exhibit streaming behaviour is typically higher than  $t_c^*$  for rebounding drops and is difficult to predict, since the detachment mechanism is totally unique from the other behaviours discussed in this report. We recommend that in future studies, this behaviour is modeled numerically in order to gain more insight on the underlying principles.

## CONCLUSIONS

In this report, we tested the influence of 5 different superhydrophobic microstructures on the restitution coefficient ( $\epsilon$ ), dimensionless maximum spreading diameter ( $D_{max}^*$ ), and dimensionless contact time ( $t_c^*$ ) of oblique water drop impacts.

Both the normal ( $\varepsilon_n$ ) and tangential restitution coefficients ( $\varepsilon_t$ ) show no dependence on the  $AOI$ , and instead are governed primarily by  $We_n$  (as per **Equation 2**).  $\varepsilon_n$  and  $\varepsilon_t$  are also independent of the surface's microstructure, which was expected for  $\varepsilon_n$  (based on established theory) but is difficult to explain for the case of  $\varepsilon_t$ . Therefore, we suggest that future studies further investigate the tangential restitution coefficient, to better understand its governing principles.

$D_{max}^*$  of oblique impacts is well described by **Equation 8**, in which the adhesion coefficient ( $c$ ) represents the adhesive properties of the surface and is linearly related to the microstructure roughness. Based on this analysis, we discovered that  $D_{max}^*$  is greater on hierarchical micro/nanostructured surfaces than on superhydrophobic surfaces patterned only with nanostructures.

Regarding  $t_c^*$ , at normal  $AOI$ , increasing  $v_n$  leads to a longer overall contact time due to the penetration of the liquid into the pores of the superhydrophobic surface. However, in oblique impacts, the presence of stretched rebounding behaviour actually leads to a negative correlation between  $v_n$  and  $t_c^*$  due to the accelerated retraction of the lamella in the lateral direction. Accordingly, the contact time of oblique impacts decreases as the impact speed increases.

Finally, drop impacts that exhibit the unique pancake bouncing behaviour do not conform to any of the trends outlined above. Notably, using a pressure balance we demonstrate that  $\varepsilon$  is especially low for pancake bouncing because the drop is propelled upwards only by capillary forces, instead of the retraction mechanism that prompts bouncing for most superhydrophobic drop impacts.

## ASSOCIATED CONTENT

Supporting Note 1. Schematic of the sample holder used to contain the P200 sample during immersion confocal microscopy.

Supporting Note 2. Map of the impact behaviour observed on all experimental surfaces, at each Weber number and angle of incidence tested.

Supporting Note 3. Normal and tangential restitution coefficients versus the normal Weber number for all 5 experimental surfaces.

Supporting Note 4. Explanation of determined value of the pre-factor  $k$  in **Equation 5**.

Supporting Note 5. Full derivation of **Equation 8**.

Supporting Note 6. Evolution of the dimensionless contact time as  $We_n$  is raised for  $AOI=30^\circ$ .

Supporting Video 1: Original video for **Figure 2(a)**.

Supporting Video 2: Original video for **Figure 2(b)**.

Supporting Video 3: Original video for **Figure 2(c)**.

Supporting Video 4: Original video for **Figure 2(d)**.

Supporting Video 5: Original video for **Figure 2(e)**.

Supporting Video 6: Four equivalent drop impacts at  $We_n = 45$  and  $AOI = 30^\circ$  occurring in tandem on the Nano, Wavy, H200, and P100 surfaces.

Supporting Video 7: Stretched rebounding behaviour for a drop impact on P200 at  $We_n = 78$  and  $AOI = 0^\circ$ .

Supporting Video 8: Synchronized side-by-side video of the above-view and side-view drop impact videos from **Figure 8(a)**.

## AUTHOR INFORMATION

### **Corresponding Author**

\*Anne-Marie Kietzig, McGill University, Department of Chemical Engineering 3610 University Street, Montreal, Quebec, H3A 0C5, Canada, email: [anne.kietzig@mcgill.ca](mailto:anne.kietzig@mcgill.ca).

### **Author Contributions**

Damon Aboud designed and performed the experiments and wrote the manuscript. Prof. Anne-Marie Kietzig guided the project and edited the manuscript. All authors have given approval to the final version of the manuscript.

### **Funding Sources**

This work was supported by the Natural Sciences and Engineering Research Council (NSERC) of Canada through the NSERC Strategic Network Green-SEAM.

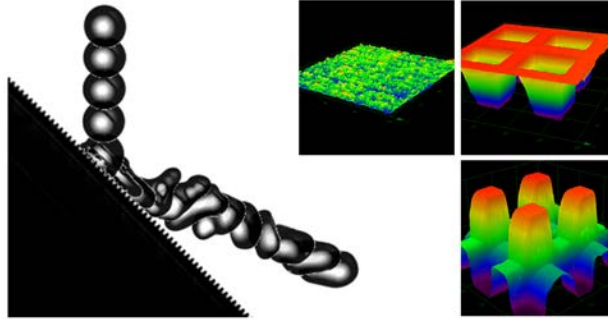
## ACKNOWLEDGMENT

The authors acknowledge the assistance of Dr. Anne-Marie Ladouceur of the McGill Advanced BioImaging Facility, who helped obtain the immersion confocal microscopy images.

## REFERENCES

1. Sarkar, D. K.; Farzaneh, M.; Technology Superhydrophobic Coatings with Reduced Ice Adhesion. *J. Adhes. Sci. Technol.* **2009**, 23, 1215-1237.
2. Park, J.; Lim, H.; Kim, W.; Ko, J. S. Design and Fabrication of a Superhydrophobic Glass Surface with Micro-Network of Nanopillars. *J. Colloid Interface Sci.* **2011**, 360, 272-279.
3. Li, X.-M.; Reinhoudt, D.; Crego-Calama, M. What Do We Need for a Superhydrophobic Surface? A Review on the Recent Progress in the Preparation of Superhydrophobic Surfaces. *Chem. Soc. Rev.* **2007**, 36, 1350-1368.
4. Barthlott, W.; Neinhuis, C. Purity of the Sacred Lotus, or Escape from Contamination in Biological Surfaces. *Planta* **1997**, 202, 1-8.
5. Clanet, C.; Béguin, C.; Richard, D.; Quéré, D. Maximal Deformation of an Impacting Drop. *J. Fluid Mech.* **2004**, 517, 199-208.
6. Biance, A.-L.; Chevy, F.; Clanet, C.; Lagubeau, G.; Quéré, D. On the Elasticity of an Inertial Liquid Shock. *J. Fluid Mech.* **2006**, 554, 47-66.
7. Aria, A. I.; Gharib, M. Physicochemical Characteristics and Droplet Impact Dynamics of Superhydrophobic Carbon Nanotube Arrays. *Langmuir* **2014**, 30, 6780-6790.
8. Mishchenko, L.; Hatton, B.; Bahadur, V.; Taylor, J. A.; Krupenkin, T.; Aizenberg, J. Design of Ice-Free Nanostructured Surfaces Based on Repulsion of Impacting Water Droplets. *ACS Nano* **2010**, 4, 7699-7707.
9. Richard, D.; Clanet, C.; Quéré, D. Contact Time of a Bouncing Drop. *Nature* **2002**, 417, 811.
10. Liu, Y.; Moevius, L.; Xu, X.; Qian, T.; Yeomans, J. M.; Wang, Z. Pancake Bouncing on Superhydrophobic Surfaces. *Nat. Phys.* **2014**, 10, 515-519.
11. Lee, C.; Nam, Y.; Lastakowski, H.; Hur, J. I.; Shin, S.; Biance, A.-L.; Pirat, C.; Ybert, C. Two Types of Cassie-to-Wenzel Wetting Transitions on Superhydrophobic Surfaces During Drop Impact. *Soft Matter* **2015**, 11, 4592-4599.
12. LeClear, S.; LeClear, J.; Park, K.-C.; Choi, W. Drop Impact on Inclined Superhydrophobic Surfaces. *J. Colloid Interface Sci.* **2016**, 461, 114-121.
13. Maitra, T.; Tiwari, M. K.; Antonini, C.; Schoch, P.; Jung, S.; Eberle, P.; Poulikakos, D. On the Nanoengineering of Superhydrophobic and Impalement Resistant Surface Textures Below the Freezing Temperature. *Nano Lett.* **2013**, 14, 172-182.
14. Aboud, D. G. K.; Kietzig, A.-M. On the Oblique Impact Dynamics of Drops on Superhydrophobic Surfaces. Part I: Sliding Length and Maximum Spreading Diameter. *Langmuir* **2018**, 34, 9879-9888.
15. Aboud, D. G. K.; Kietzig, A.-M. On the Oblique Impact Dynamics of Drops on Superhydrophobic Surfaces. Part II: Restitution Coefficient and Contact Time. *Langmuir* **2018**, 34, 9889-9896.
16. Aboud, D. G. K.; Kietzig, A.-M. Splashing Threshold of Oblique Droplet Impacts on Surfaces of Various Wettability. *Langmuir* **2015**, 31, 10100-10111.
17. Assaf, Y.; Zhao, M.; Kietzig, A.-M. Femtosecond Laser-Induced Porosity on Poly (Ethylene) Surfaces—a Crystallographic and Rheological Study. **2018**, 124, 023103.
18. Liang, F.; Lehr, J.; Danielczak, L.; Leask, R.; Kietzig, A.-M. Robust Non-Wetting Ptfе Surfaces by Femtosecond Laser Machining. *Int. J. Mol. Sci.* **2014**, 15, 13681-13696.

19. Aboud, D. G. K. Oblique Drop Impacts on Superhydrophobic Surfaces. Ph.D. thesis, McGill University, Montréal, 2018.
20. Gilet, T.; Bush, J. W. Droplets Bouncing on a Wet, Inclined Surface. *Phys. Fluids* **2012**, 24, 122103.
21. Wenzel, R. N. Resistance of Solid Surfaces to Wetting by Water. *Industrial & Engineering Chemistry* **1936**, 28, 988-994.
22. Bhushan, B.; Nosonovsky, M. The Rose Petal Effect and the Modes of Superhydrophobicity. *Philosophical Transactions of the Royal Society A: Mathematical, Physical and Engineering Sciences* **2010**, 368, 4713-4728.
23. Wang, H.; Liu, C.; Zhan, H.; Liu, Y. Droplet Asymmetric Bouncing on Inclined Superhydrophobic Surfaces. **2019**, 4, 12238-12243.
24. Zhang, R.; Hao, P.; He, F. Drop Impact on Oblique Superhydrophobic Surfaces with Two-Tier Roughness. *Langmuir* **2017**, 33, 3556-3567.



**TOC Graphic**